

# Power asymmetry in CMB polarization maps from PLANCK : a local variance analysis

Pavan K. Aluri<sup>1,2\*</sup>, Arman Shafieloo<sup>2,3†</sup>

January 30, 2022

<sup>1</sup>Korea Institute for Advanced Study (KIAS), Quantum Universe Center (QUC),  
85 Hoegi-ro, Dongdaemun-gu, Seoul - 02455, Republic of Korea

<sup>2</sup>Korea Astronomy and Space Science Institute (KASI),  
Yuseong-gu, 776 Daedeok daero, Daejeon 34055, Republic of Korea

<sup>3</sup>University of Science and Technology (UST),  
Yuseong-gu 217 Gajeong-ro, Daejeon 34113, Republic of Korea

## Abstract

A persistent signal of power asymmetry on opposite hemispheres of CMB sky was seen in full-sky temperature measurements made so far. This asymmetry was seen in microwave sky from WMAP as well as PLANCK satellites, and calls for attention the larger question of *statistical isotropy*, one of the foundational principles of modern cosmology. In this work we present an analysis of polarized CMB maps from PLANCK 2015 full mission data. We apply the local variance estimator on low resolution  $E$ -mode maps from PLANCK 2015 polarization **Commander** solution. We find a significant hemispherical power asymmetry in polarization data on large angular scales, at the level of  $\sim 2.6 - 3.9\%$  depending on the galactic mask, and the circular disc radius used for computing local variance maps. However the direction is found to be pointing broadly towards CMB kinetic dipole direction. Precise measurements of CMB polarization in future will shed light on this apparent discrepancy in the anisotropy axis seen in temperature and polarized CMB sky, and likely influence of systematics on our findings.

## 1 Introduction

Hemispherical power asymmetry (HPA), initially observed in WMAP first year temperature data [1] has come to be one of the outstanding anomalies that indicated violation of *statistical isotropy* on large angular scales of CMB sky. This anisotropic signal persisted between completely different full-sky missions viz., WMAP and PLANCK probes, that involved different analysis procedures, systematics and science teams [2, 3, 4]. HPA attracted significant attention from the cosmology community, which was estimated using a variety of methods, see for example Ref. [5, 6, 7, 8, 9, 10, 11, 12, 13, 14, 15, 16, 17, 18, 19, 20, 21, 22, 23, 24, 25]. Many explanations were also put forth to explain this anomaly with no final conclusion.

This hemispherical power asymmetry has come to be modelled as a dipole modulation of otherwise statistically isotropic CMB sky as [26, 27],

$$\Delta\tilde{T}(\hat{n}) = \Delta T(\hat{n})(1 + A \hat{\lambda} \cdot \hat{n}), \quad (1)$$

where  $\Delta\tilde{T}(\hat{n})$  and  $\Delta T(\hat{n})$  are the modulated/observed and statistically isotropic CMB anisotropy fields respectively in the direction  $\hat{n}$ .  $A$  and  $\hat{\lambda}$  are the amplitude and direction of modulation.

---

\*aluri@kasi.re.kr

†shafieloo@kasi.re.kr

Here the amplitude can be scale dependent [3, 4, 18, 20, 24, 25]. This phenomenological modelling of HPA as dipole modulation of temperature field has important implications for the statistics of observed CMB signal. It induces off-diagonal correlations in the two-point function that couples a multipole  $l$  to  $l' = l \pm 1$ . These correlations were exploited to estimate the anisotropic signal itself [3, 4, 7, 14, 18, 24, 23, 25].

In this paper, we probe the presence of hemispherical power asymmetry in the polarized CMB signal from PLANCK full mission data. The PLANCK science team didn't report any analysis of PLANCK 2015 CMB polarization maps in the context of isotropy studies. As the PLANCK papers inform [28], this is because of the uncertainty in the level of recovered polarization signal on large angular scales, that warrants such analysis. Accordingly the low multipoles of polarized CMB signal in the various component separated CMB polarization maps have been excluded in the full mission PLANCK data that is made public. Further the complimentary simulations to polarization data that are also made public, have a significant level of mismatch in the noise level compared to data. However in this paper, we work in the lower to intermediate range of multipoles, and suitably modifying the noise simulations, that are already made available through the second public release to compute significances.

## 2 CMB polarization maps

The CMB temperature anisotropies are conventionally expanded in terms of spherical harmonics as

$$\Delta T(\hat{n}) = \sum_{l=2}^{\infty} \sum_{m=-l}^l a_{lm}^T Y_{lm}(\hat{n}), \quad (2)$$

where  $\Delta T(\hat{n})$  are temperature anisotropies after subtracting the leading monopole and dipole components in the sky direction  $\hat{n}$ ,  $a_{lm}^T$  are the coefficients of expansion, and  $Y_{lm}(\hat{n})$  are a suitable basis to expand the temperature anisotropies on a sphere.

Unlike the intensity field, CMB polarization stokes  $Q/U$  parameters are not scalars under rotation and are frame dependent. The combination  $X_{\pm}(\hat{n}) = (Q \pm iU)(\hat{n})$  transforms as  $X'_{\pm}(\hat{n}) = e^{\mp 2i\psi} (Q \pm iU)(\hat{n})$ , under rotation by an angle  $\psi$  of the co-ordinate plane perpendicular to the direction  $\hat{n}$  in which  $Q/U$  are defined. Hence  $X_{\pm}(\hat{n})$  transform as a spin  $\pm 2$  field under coordinate transformations. Thus it is expanded in terms of spin-weighted spherical harmonics,  ${}_sY_{lm}$ , as

$$X_{\pm}(\hat{n}) = (Q \pm iU)(\hat{n}) = \sum_{l=2}^{\infty} \sum_{m=-l}^l a_{\pm 2, lm} {}_{\pm 2}Y_{lm} \hat{n}, \quad (3)$$

where  ${}_{\pm 2}Y_{lm}(\hat{n})$  are the spin-2 spherical harmonics, and  $a_{\pm 2, lm}$  are the coefficients of expansion in that basis [29, 30, 31, 32].  $Y_{lm} = {}_0Y_{lm}$  are the usual spherical harmonics that are used to decompose the CMB temperature field which is a spin-0 field.

Further, a linear combination of these spin-2 spherical harmonic coefficients,  $a_{\pm 2, lm}$ , can be defined as [30, 32]

$$a_{lm}^E = -(a_{2, lm} + a_{-2, lm})/2 \quad \text{and} \quad (4)$$

$$a_{lm}^B = -(a_{2, lm} - a_{-2, lm})/2i, \quad (5)$$

where  $a_{lm}^E$  and  $a_{lm}^B$  are respectively called *electric* and *magnetic* modes of polarization that are invariant under rotations. Similar to an electric and magnetic field,  $a_{lm}^E$  and  $a_{lm}^B$  respectively have even and odd parity properties under inversion i.e., for  $\hat{n} \rightarrow -\hat{n}$ ,  $a_{lm}^E \rightarrow (-1)^l a_{lm}^E$  and  $a_{lm}^B \rightarrow (-1)^{l+1} a_{lm}^B$ . Thus one can obtain two spin-0 fields as

$$E(\hat{n}) = \sum_{lm} a_{lm}^E Y_{lm}(\hat{n}) \quad \text{and} \quad B(\hat{n}) = \sum_{lm} a_{lm}^B Y_{lm}(\hat{n}). \quad (6)$$

As mentioned above, owing to their parity properties under inversion,  $E(\hat{n})$  is a scalar field while  $B(\hat{n})$  is a pseudo-scalar field. Physically these modes originate from distinct sources. Whereas, scalar perturbations give rise to purely  $E$ -modes, only tensor perturbations can generate  $B$ -modes (on large angular scales). Lensing due to large scale structure can induce  $B$ -modes from  $E$ -modes at small angular scales.

In this paper, we test for hemispherical power asymmetry in CMB  $E$ -mode maps derived from PLANCK full mission data.

### 3 Methodology and Data sets

#### 3.1 Local variance estimator

We use the recently proposed local variance estimator (LVE) that was applied to probe hemispherical power asymmetry in temperature data [20]. This statistical approach is based on the Crossing statistic that has been proposed to address some different problems in astronomy [33, 34, 35, 36].

Hereafter we use LV or LVE to refer to local variance analysis or maps thus estimated. In this section, we briefly describe the LV method to apply on polarized CMB maps.

One can define a variance map of the observed CMB temperature sky as,

$$\sigma_r^2(\hat{N}) = \sum_{p \in r @ \hat{N}} (T(p) - \bar{T}_r)^2, \quad (7)$$

where  $\sigma_r^2$  is the variance computed locally from all the pixels  $p$ , falling inside a circular disc of chosen radius  $r$  defined in the sky direction  $\hat{N}$ , and  $\bar{T}_r$  is the mean temperature corresponding to the same circular region.

A variance map of dipole modulated CMB sky following Eq. [1] is given by

$$\tilde{\sigma}^2(\hat{N}) \approx \sigma^2(\hat{N})(1 + 2 A \hat{\lambda} \cdot \hat{N}), \quad (8)$$

upto first order in the isotropy violating dipole field, where  $\tilde{\sigma}^2$  and  $\sigma^2$  are maps of locally computed variances of modulated and unmodulated CMB anisotropies respectively. Further, a normalized variance map is constructed as

$$\xi(\hat{N}) = \frac{\sigma_{obs}^2(\hat{N}) - \langle \sigma^2(\hat{N}) \rangle}{\langle \sigma^2(\hat{N}) \rangle}, \quad (9)$$

where  $\langle \sigma^2(\hat{N}) \rangle$  is the expected mean field bias in variance estimated from CMB simulations (including inhomogeneous noise), that is subtracted from the local variance map of the observed sky. From this normalized variance map we compute the dipole amplitude (and direction) to check for consistency with random expectations for any given realization. Any significant dipole amplitude thus found in data would indicate a significant hemispherical power asymmetry, hemisphere defined by the corresponding dipole direction, and hence a breakdown of statistical isotropy. We should note that one can define different metrics to test the statistical isotropy using the normalized variance map but in this work we focus on the dipole amplitude and its direction.

In practice, one implements the local variance estimator as follows. Any cleaning procedure to clean the raw satellite data, is limited by the level of foreground emission in a given sky region. Correspondingly, owing to high emission levels in the galactic plane, the recovered CMB signal is less reliable in those regions. Bright point and extended sources of extragalactic origin also lead to the same situation. Thus these regions are masked in any CMB analysis to avoid biases due to residual foreground contamination. Hence, in computing the local variances at different sky locations, the circular disc mask defined locally is taken in union with the galactic mask

to exclude potentially contaminated regions of the recovered CMB sky. Further to make the analysis robust, we can define a criterion for using these locations only if a chosen fraction of the sky pixels, say for example 50% or 80%, in comparison to the number of pixels available using the full disc mask, survive in the effective disc mask (ie., the union of galactic mask and the locally defined circular disc mask of a chosen radius). Thus, the fraction of the sky over which local variances are computed is less than the sky fraction of the galactic mask used to omit regions with potential residual contamination. Operationally, we set these invalid pixels to the **HEALPix** bad value  $= -1.6375 \times 10^{30}$ . And a dipole is fit to the (normalized) local variance map thus obtained using only the valid pixels.

To analyze the polarization maps, we apply the LV estimator to the  $E$ -mode map (defined by Eq. [6]). The variance is computed as  $\sigma_r^2(\hat{N}) = \langle E^2(p) \rangle_{p \in r @ \hat{N}}$ , where the angular brackets denote the average of the squared  $E$ -mode field computed using all pixels,  $p$ , falling inside an effective circular disc of chosen radius,  $r$ , defined at  $\hat{N}$  on the CMB sky.

## 3.2 Data sets used

### 3.2.1 $E$ -mode CMB maps

We do our local variance analysis on a CMB  $E$ -mode map. To this extent we use the full-sky Stokes  $Q$  and  $U$  CMB maps from PLANCK full mission data, estimated using the **Commander** algorithm. These  $Q/U$  maps are made available through PLANCK's second public release<sup>1</sup>. Using partial skies to go from  $Q/U$  to  $E/B$  basis, will induce undesired correlations due to masking in the resultant maps. Hence we use full-sky polarization maps to obtain  $E$ -map. PLANCK also employed other component separation schemes viz., NILC, SEVEM, and SMICA [28] to extract CMB signal from raw satellite data. But the recovered Stokes  $Q/U$  CMB maps from these other methods have a portion of the sky removed, or some visible contamination still present, in the galactic region. Hence we use only the **Commander** Stokes  $Q$  and  $U$  maps to get full-sky  $E$ -mode map in this work. Note that we eventually use galactic mask in our studies which excise unreliable regions of the recovered CMB sky from raw data using PLANCK provided polarization mask. We also make use of custom-made polarization masks, as explained later.

The **Commander** estimated  $Q/U$  maps are available at **HEALPix**  $N_{side} = 1024$  with smoothing given by a Gaussian beam of  $FWHM = 10'$  (arcmin). Since the polarized CMB maps are dominated by noise at high- $l$ , in this paper we work with a low resolution  $E$ -mode map at  $N_{side} = 256$  with a beam resolution of  $FWHM = 40'$  (arcmin) Gaussian beam. First the **HEALPix** facilities - **anafast** and **alteralm** - are applied in succession to obtain  $E/B$   $a_{lm}$ 's from Stokes  $Q/U$  maps, at the desired lower beam/pixel resolution.

Now, as mentioned earlier, various component separated maps have their low- $l$  modes removed in the maps that are made publicly available. This is so because of the unsatisfactory level of systematic artefacts still present on large angular scales of PLANCK polarization maps [28]. A window function in multipole space defined as

$$f_l = \begin{cases} 0 & \forall \quad l < l_1 \\ \frac{1}{2} \left( 1 - \cos \left( \pi \frac{l-l_1}{l_2-l_1} \right) \right) & \forall \quad l_1 \leq l \leq l_2 \\ 1 & \forall \quad l > l_2 \end{cases} \quad (10)$$

where  $l_1 = 20$  and  $l_2 = 40$ , is applied to these publicly released CMB maps. Further as discussed in Appendix A, to reduce the effect of noise dominated modes in the CMB  $E$ -mode map thus

<sup>1</sup>[http://irsa.ipac.caltech.edu/data/Planck/release\\_2/all-sky-maps/matrix\\_cmb.html](http://irsa.ipac.caltech.edu/data/Planck/release_2/all-sky-maps/matrix_cmb.html)

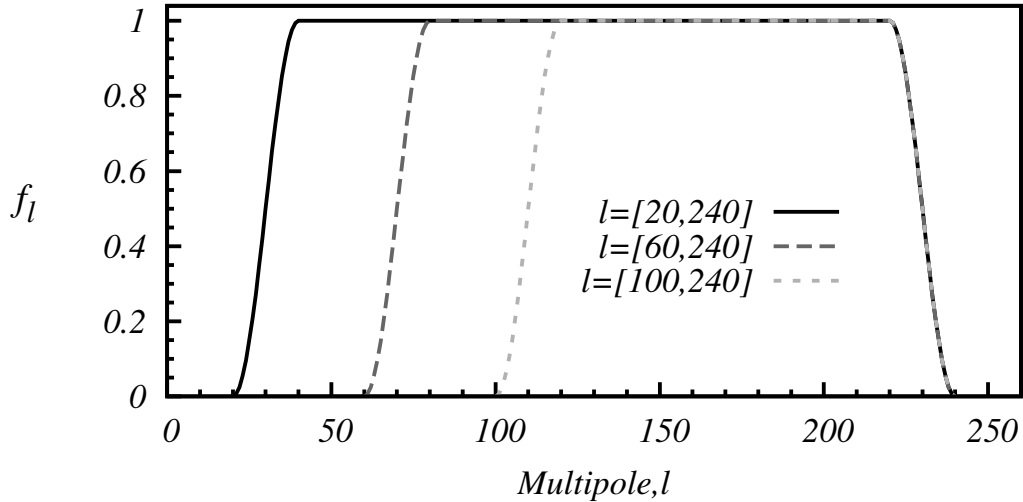


Figure 1: Three different high-pass filters used to produce  $E$ -mode CMB maps, all with a fixed low-pass filter are shown here. These different filters are applied to produce polarized  $E$ -maps comprising different angular scales to probe for any scale dependence in the amplitude of dipole, fit to the derived local variance maps. At high- $l$ , the low-pass filter is applied to smoothly suppress the effect of noisy modes in data. See text for details.

obtained on our analysis, we additionally apply a similar cosine filter at high- $l$  as

$$f_l = \begin{cases} 1 & \forall \quad l < l_1 \\ \frac{1}{2} \left[ 1 + \cos \left( \pi \frac{l-l_1}{l_2-l_1} \right) \right] & \forall \quad l_1 \leq l \leq l_2 \\ 0 & \forall \quad l > l_2 \end{cases} \quad (11)$$

where  $l_1 = 220$  and  $l_2 = 240$ .

The hemispherical power asymmetry, as found in CMB temperature data is present significantly on the large angular scales viz.,  $l \lesssim 64$  [3, 4, 14, 18, 24, 23, 25]. In order to test for similar behaviour in the polarized CMB map, we do additional high pass filtering to get two  $E$ -mode CMB maps using the window function defined by Eq. [10] with  $l_1 = 60/l_2 = 80$  and  $l_1 = 100/l_2 = 120$  at low- $l$ . The various  $l$ -space windows used to produce the filtered  $E$ -mode CMB maps are shown in Fig. [1].

These filtered  $E$ -mode  $a_{lm}$ 's are then converted to an  $E$ -mode map as

$$E(\hat{n}) = \sum_{lm} f_l a_{lm}^E Y_{lm}(\hat{n}) \quad (12)$$

using HEALPix facility `synfast`. Thus, in the current study, we use three different high pass filtered CMB  $E$ -mode maps as derived from PLANCK provided Stokes  $Q/U$  maps estimated using `Commander` algorithm. They have a beam resolution given by a Gaussian beam of  $FWHM = 40'$  (arcmin) and at  $N_{side} = 256$ , comprising different angular modes.

### 3.2.2 Masks

Common galactic masks for polarization analysis were provided by the PLANCK team through their second data release<sup>2</sup> at HEALPix  $N_{side} = 1024$ . The confidence masks provided by the individual component separation methods were combined to obtain a union mask which would be the most conservative mask for CMB analysis irrespective of the specific component separation

<sup>2</sup>[http://irsa.ipac.caltech.edu/data/Planck/release\\_2/ancillary-data/](http://irsa.ipac.caltech.edu/data/Planck/release_2/ancillary-data/)

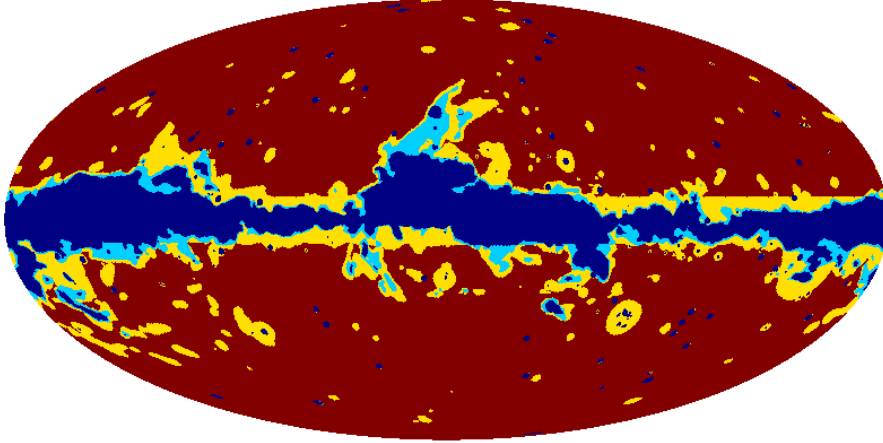


Figure 2: Various polarization masks used in the present work are shown here. These are created in  $P$ -space where  $P^2 = \sqrt{Q^2 + U^2}$ . The *deep blue* region is excluded by all masks. The *red* region corresponds to a mask derived by downgrading PLANCK’s UPB77 mask, which has an  $f_{sky} \approx 74\%$ . The *light blue* and *yellow* regions (including *red*) are our custom made polarization masks which have an available sky of  $\approx 80\%$  and  $85\%$  respectively. These three masks are referred to as `mask074`, `mask080`, and `mask085` respectively. Point sources are also accounted for in these masks.

method used to extract CMB signal. This union mask (referred as UP78) was further extended to obtain two versions UPA77 and UPB77. We use the UPB77 mask in the current work, which was deemed more reliable than the other in handling point source contamination. This mask UPB77 has a sky fraction of  $\approx 77\%$ . See Ref. [28] for more details regarding PLANCK galactic masks.

Since we work at low resolution of HEALPix  $N_{side} = 256$ , the UPB77 mask is downgraded as follows. The high resolution mask is available at HEALPix  $N_{side} = 1024$ . We first invert this mask and fill all island like regions inside using the HEALPix facility `process_mask`. To be more conservative, these island like regions in the galactic region are excluded to begin with. This inverted/filled high resolution mask is downgraded to  $N_{side} = 256$ . Then a Gaussian beam of  $FWHM = 40'$  (arcmin) is applied, which is same as that of the CMB map we analyse. Finally a cut-off of 0.05 is applied on this inverted, filled, downgraded, and smoothed mask where those pixels with pixel-value less than this cut-off are set to ‘1’, and ‘0’ otherwise. We do so, so as to be able to handle leakage due to smearing of extended/point source contamination due to smoothing. The mask thus obtained has a sky fraction of  $f_{sky} \approx 0.74$ . This mask is referred to as `mask074`, and is shown in *red* in Fig. [2].

Now the confidence masks for individual component separated CMB polarization maps have an available sky fraction of  $\approx 83\%$ ,  $96\%$ ,  $79\%$  and  $85\%$  respectively for **Commander**, **NILC**, **SEVEM**, and **SMICA** derived solutions. Their mask contours are different, and hence they excise different regions of the sky. So, we further devise two more masks with larger sky fraction for use in this analysis as follows. Here we adopt the procedure of Tegmark et al. (2003) [37], used to define sky partitions for iterative cleaning of the CMB sky. To create these additional masks, we use the raw polarization maps of PLANCK 030, 070 and 353 GHz channels. These maps with different beam/pixel smoothing and map resolution are first downgraded to have a common beam, pixel and map resolution. The raw  $Q/U$  maps corresponding to each of these three frequencies are deconvolved with their respective circular beam transfer functions, and simultaneously smoothed with a Gaussian beam of  $FWHM = 2^\circ$  (degrees), so as to have largely contiguous regions in the masks being created, while repixelizing them at a lower resolution of  $N_{side} = 256$ . Among the PLANCK frequency channels, the 070 GHz band has visibly lowest foreground levels in the raw satellite data. The raw map corresponding to this frequency band is subtracted from the



lowest and highest frequency raw maps from PLANCK that are sensitive to polarization viz., the 030 and 353 GHz channels. These two difference maps, 030–070 and 353–070, in  $Q/U$  basis containing only foregrounds, are dominated by synchrotron and thermal dust respectively. The individual difference maps in  $Q/U$  are further combined to form  $P$ –maps, where  $P^2 = Q^2 + U^2$ . These two  $P$ –maps, are then used to create what is called a *junk map* which retains only the pixel-value that is largest between the two  $P$ –maps at any sky location. This junk map taken as representative of the maximum foreground signal in any sky direction due to any polarized non-CMB emission is thresholded at different values to obtain galactic masks with different sky fractions. Thus a suitable cut-off is applied to this junk map to obtain two more galactic masks that have a sky fraction of 80% and 85%, respectively.

In order to account for the point source contamination, we extend the point source masks in polarization as provided by PLANCK team at different frequencies<sup>3</sup>. The point source masks that are available at  $N_{side} = 2048$  at different frequency bands are first added together to make a composite polarized point source mask. This composite mask at higher  $N_{side}$  is then processed similar to the galactic masks described above to obtain an extended composite point source mask at low resolution of  $N_{side} = 256$  that is then applied to the two galactic masks we created viz., `mask080` and `mask085`. Although the addition of point sources reduces the sky fraction, we continue to refer to them as `mask080` and `mask085`. The *yellow* and *light blue* regions (along with *red* region) shown in Fig. [2], correspond to these two masks respectively.

Thus we have three masks labelled `mask074`, `mask080`, and `mask085` which have respectively  $f_{sky} \approx 74\%$ ,  $80\%$ , and  $85\%$  unmasked sky fractions. The LVE maps are obtained using these three foreground exclusion masks. We additionally created two more masks in  $E$ –basis, and the whole LV analysis is repeated using these  $E$ –masks as test of robustness of our analysis using  $P$ –masks.

### 3.2.3 Simulations

Here we describe the generation of simulations used to supplement the clean polarized CMB maps from satellite observations for computing significances.

PLANCK team provided a set of 1000 CMB maps at each frequency band in which it made observations of polarized microwave sky, that have same instrument properties such as beam smoothing similar to the observed maps. Also provided are a set of 1000 inhomogeneous noise maps corresponding to each of the seven frequency bands (030 - 353 GHz). These are called Full Focal Plane (FFP) simulations. However the PLANCK collaboration didn't make available, a similar set of processed CMB maps with noise, that complement polarized CMB sky recovered from data using various component separation methods. Hence we process the high resolution CMB and noise FFP simulations provided, to suitably obtain mock maps that augment the observed  $E$ –mode CMB maps used in the present study.

The frequency specific Stokes  $Q/U$  CMB and noise maps are available at a HEALPix resolution of  $N_{side} = 1024$  or  $2048$ , and have different beam smoothing, depending on the frequency channel. Hence all these maps are brought to a lower resolution of  $N_{side} = 256$ , and to have beam resolution given by a Gaussian beam with  $FWHM = 40'$  (arcmin) following the procedure outlined in Sec. [3.2.1] (ie., applying HEALPix facilities `anafast` and `alteralm` in sequence). In this process, we used the polarization circular beam transfer functions ( $b_l$ ) for deconvolution, that are also provided with PLANCK's second public release<sup>4</sup>. The polarized spherical harmonic coefficients,  $a_{lm}^E$ , of a simulated CMB map thus obtained are converted to an  $E$ –mode map using the HEALPix facility `synfast`.

The polarization (inhomogeneous) noise maps are also subjected to the same procedure to obtain low resolution  $E$ –mode noise maps. Now, the smoothed/downgraded  $E$ –mode noise

<sup>3</sup>[http://irsa.ipac.caltech.edu/data/Planck/release\\_2/ancillary-data/](http://irsa.ipac.caltech.edu/data/Planck/release_2/ancillary-data/)

<sup>4</sup>[http://irsa.ipac.caltech.edu/data/Planck/release\\_2/ancillary-data/](http://irsa.ipac.caltech.edu/data/Planck/release_2/ancillary-data/)

maps are combined to obtain noise r.m.s maps corresponding to each channel at  $N_{side} = 256$ . These noise r.m.s maps are then used to obtain a set of 1000 mock maps following inverse noise variance addition of  $E$ -mode CMB and noise maps corresponding to different frequency channels with same simulation/seed number<sup>5</sup>.

However the effective noise maps thus obtained are not yet useful due to an underestimation of noise in FFP simulations compared to data. As described in Appendix A, we do a rescaling of the effective noise maps by a constant multiplicative factor  $\approx 1.32$ . Thus a set of 1000 mock CMB  $E$ -mode maps with noise are generated complementing the observational data. These co-added low resolution  $E$ -mode CMB maps with (scaled) noise are further filtered using the high and low pass cosine filters defined in Eq. [10] and [11]. Thus from each co-added *realistic*  $E$ -mode CMB realization, we obtain three filtered maps similar to the observed data maps described in Sec. [3.2.1].

## 4 Results

In the present analysis, we use a CMB  $E$ -mode map derived from PLANCK 2015 Stokes  $Q/U$  CMB maps, estimated using **Commander** algorithm. Different window functions in multipole space are applied to this  $E$ -mode CMB map to get three filtered maps, as described in Sec. [3.2.1]. In order to probe any scale dependent behaviour of the amplitude of hemispherical power asymmetry, if present, that is modelled as dipole modulation of otherwise statistically isotropic CMB anisotropies, we generated these three filtered maps. All the three maps have a low-pass cosine filter applied with  $l_1/l_2 = 220/240$  following Eq. [11]. A high-pass cosine filter defined by Eq. [10] with  $l_1/l_2 = 20/40, 60/80$  and  $100/120$  are applied to obtain the said three filtered  $E$ -mode CMB maps. Note that the  $l_1/l_2 = 20/40$  filter is already applied by PLANCK team to the publicly released polarization CMB maps. We only generated the later two filtered CMB  $E$ -maps. As a consistency check of our results, we also performed the LV analysis on large angular scales using foreground masks derived in  $E$ -space directly.

### 4.1 Power asymmetry on large angular scales

Here we present results from analyzing the CMB maps containing large angular scales i.e., using the filtered  $E$ -mode CMB map comprising the multipoles  $l = [20, 240]$ . We used four different circular disc of radii  $120', 90', 60'$  and  $45'$  (arcmin), to compute local variances. The largest angular mode that is fully available in the polarized CMB map from the second data release is  $l = 40$ , and corresponds to an angular size of  $\theta = 180^\circ/l = 180^\circ/40 = 4.5^\circ$  (degrees). So we limit to using a maximum disc radius of  $2^\circ$  (degrees) i.e., a maximum circular disc of diameter  $4^\circ$  (degrees). The circular discs of different radii are defined at the pixel centers of a **HEALPix** grid of  $N_{side} = 64$ , to compute the local variances. An  $N_{side} = 64$  map has pixels of size  $a = \sqrt{4\pi/(12 \times 64^2)} \approx 55'$  (arcmin) assuming them to be a square of side  $a$ . Later on we also use two more filtered  $E$ -mode CMB maps, and given the angular scales they contain, we compute all the local variance maps using different disc radii at the same **HEALPix** resolution of  $N_{side} = 64$ . In practice the local variances are computed from effective circular discs meaning the circular discs defined locally are taken in conjugation with a galactic mask to avoid potential foreground bias on our analysis. We compute local variances only if the effective discs have

---

<sup>5</sup>In the absence of foregrounds, an ILC procedure will reduce to an inverse noise variance weighing if the pixels are uncorrelated i.e.,  $E_{co-add}(p) = \sum_{i=1}^{N_c} w_i(p) E_i(p) / \sum_{i=1}^{N_c} w_i(p)$ , where  $i$  denotes the  $N_c (= 7)$  frequency channels,  $w_i(p) = 1/\sigma_i^2(p)$  are the weights which are given by the inverse of r.m.s squared of smoothed/downgraded polarized noise maps at  $N_{side} = 256$  at each frequency, and  $p$  denoted a pixel/sky direction in the sky. Hence ignoring the correlations between pixels due to beam, we used the diagonal approximation to the noise covariance matrix to obtain suitable simulations that complement the observed maps. This is justified following our interest in probing large angular scales of the polarized CMB sky. However the effective polarization noise maps thus obtained from FFP simulations are still not usable due to an additional complication. See text for more details.



atleast 90% of the pixels in comparison to those in full disc so that our statistics are robust. This results in local variance maps with less sky fraction than the galactic mask itself used to exclude regions with potential galactic contamination in the data map. The three  $P$ -masks shown in Fig. [2] are used in the present study.

The filtered **Commander** 2015  $E$ -mode CMB map comprising the large angular scales as available, is used to compute four local variance maps at  $N_{side} = 64$ , following Eq. [7], corresponding to the choice of four circular disc of radii  $120'$ ,  $90'$ ,  $60'$  and  $45'$  (arcmin) described earlier. These LV maps are further corrected for and normalized using *mean field bias* computed from simulations. Thus we obtain normalized local variance maps as defined by Eq. [9]. A dipole is then fit to these normalized local variance maps from data, assuming that the power asymmetry, if any, is dipolar ( $L = 1$ ) in nature. We eventually check for presence of any significant power in higher modes ( $L > 1$ ) of local variance maps, that could be inducing power asymmetry.

In order to compute the *mean field bias* to correct the local variance maps from data, we proceed as follows. The generation of simulations with same beam smoothing and consistent noise levels as data, are described in Section [3.2.3] and Appendix [A]. The simulations thus obtained are filtered to contain the same multipole range as data by applying the high and low pass cosine filters following Eq. [10], [11] and [12].

We then apply the local variance estimator to simulations similar to data i.e., computing local variance maps at **HEALPix**  $N_{side} = 64$  with the same choice of circular disc radii and effective disc fraction of 90% described above, from each simulation. Thus a set of 1000 local variance maps are derived, corresponding to each of the circular disc radii chosen and the galactic mask used. A *mean field* is thus estimated by taking the mean of the 1000 LV maps from simulations for each choice of disc radius and mask. This is subtracted from and also used to normalize the data LV maps (Eq. [12]). The simulations themselves are also normalized using the mean field LV estimate.

The amplitudes of dipole power asymmetry in data in comparison to simulations are shown in Fig. [3]. The four plots in that figure correspond to the four choices of disc radii made to compute the local variances across the sky. The *red*, *green* and *blue* histograms in each plot of the figure correspond to the three  $P$ -masks described in the previous section (Fig. [2]). The amplitude of dipole in LV maps from data are denoted by triangle point types in each plot. We used the **HEALPix** subroutine `remove_dipole` to obtain the dipole amplitudes and directions from data and simulations. An estimate of the variance of the normalized local variance maps from isotropic simulations is used for inverse noise variance weighing of pixels to compute the dipole amplitudes and directions from normalized LV maps while using the subroutine `remove_dipole`. The dipole amplitudes as well as probability-to-exceed the observed values ( $p$ -values) corresponding to different choices of circular disc radii for mapping the local variances in **Commander** 2015 CMB  $E$ -mode map comprising large angular scales ( $l = [20, 240]$ ) are tabulated in the top block of Table 1. The three rows in that block correspond to the three  $P$ -masks used. The dispersion in recovered dipole amplitudes from corresponding simulations are quoted as errors in braces in the table.

As can be readily noticed from Fig. [3], the amplitude of dipole in normalized LV maps from data denoted by triangle point types are significantly anomalous with a probability,  $p < 1/1000$ . So none of the 1000 normalized local variance maps from simulations have a dipole of amplitude more than that seen in data. Further a careful observation also reveals that when using smaller disc radii, the distance between data points and the footsteps of the histogram on the right increases, in comparison to using disc radius of  $120'$  (arcmin). From Table 1, we also see that the amplitudes are consistent with each other, rather independent of the galactic mask used which have different masking fractions, as well as the disc radius chosen to compute local variances.

The direction of the dipoles as inferred from these normalized local variance maps are

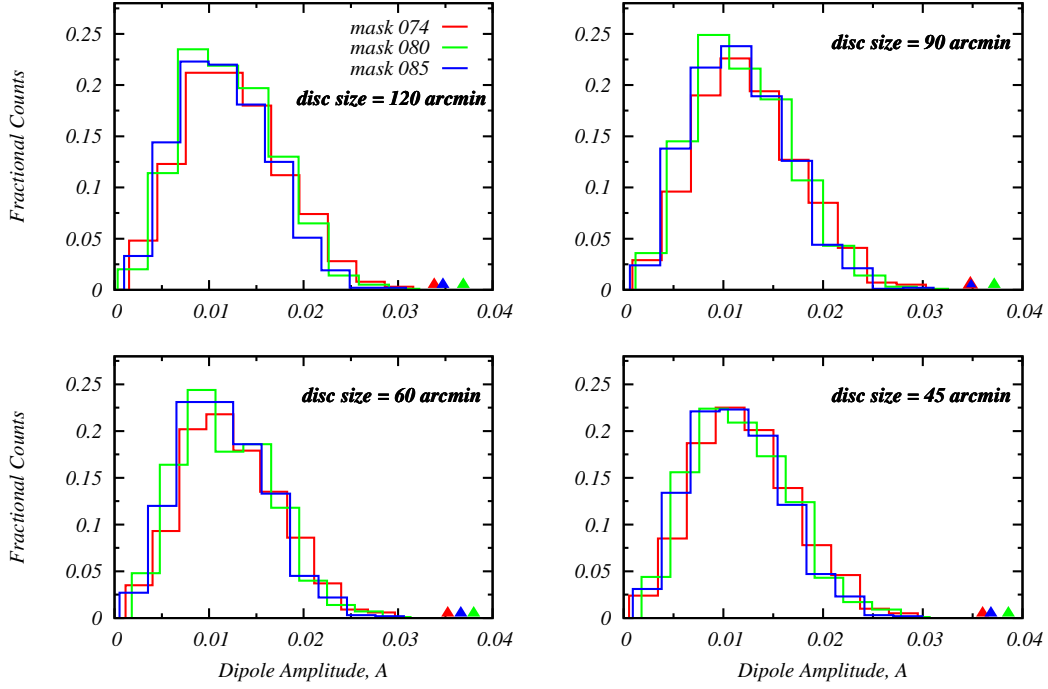


Figure 3: Histograms of amplitude of dipole, fit to the normalized local variance maps from simulated  $E$ -mode CMB maps are shown here, in comparison to data values (denoted by small triangles in each plot). The  $E$ -mode polarization map comprising the multipole range  $l = [20, 240]$  is analyzed here using four circular discs of radii  $120'$ ,  $90'$ ,  $60'$  and  $45'$  (arcmin), defined locally in each sky direction for computing local variances. Each plot has three histograms that correspond to the three  $P$ -masks with different sky fractions, used to estimate the LV maps.

$l$ -range	ds= $120'$ $A$ , $p$ -value	ds= $90'$ $A$ , $p$ -value	ds= $60'$ $A$ , $p$ -value	ds= $45'$ $A$ , $p$ -value
$l = [20, 240]$	0.034(10), 0.000	0.035(10), 0.000	0.035(10), 0.000	0.036(10), 0.000
	0.037(10), 0.000	0.037(10), 0.000	0.038(10), 0.000	0.039(10), 0.000
	0.035(10), 0.000	0.035(10), 0.000	0.037(9), 0.000	0.037(9), 0.000
$l = [60, 240]$	-	0.028(11), 0.007	0.028(11), 0.006	0.028(10), 0.003
	-	0.028(10), 0.005	0.029(10), 0.001	0.029(10), 0.000
	-	0.026(10), 0.006	0.028(10), 0.002	0.028(10), 0.001
$l = [100, 240]$	-	0.019(11), 0.173	0.018(11), 0.166	0.018(11), 0.165
	-	0.017(11), 0.219	0.018(11), 0.168	0.019(11), 0.134
	-	0.018(10), 0.148	0.019(10), 0.106	0.020(10), 0.086

Table 1: The amplitude of dipole, fit to normalized local variance maps, as obtained from PLANCK full mission **Commander** solution derived  $E$ -mode CMB map, are tabulated here. The first column lists the available multipole modes in the filtered CMB polarization maps as used in the present analysis, that correspond to probing HPA at different angular scales. Rest of the columns denote the four circular disc radii, as indicated, that are chosen to compute variances locally on the input map. The three sub-rows under any  $l$ -range denote the amplitude and its  $p$ -value as estimated using the three masks with 74%, 80% and 85% available sky fractions respectively. Note that the amplitude quoted here is ' $A$ ' as referred to in Eq. [1] and [8]. Quoted in braces are the error upto the last digits as indicated in the observed value of the dipole amplitude.

$l$ -range	ds=120' ( $\ell^\circ, b^\circ$ ) $\theta^\circ$	ds=90' ( $\ell^\circ, b^\circ$ ) $\theta^\circ$	ds=60' ( $\ell^\circ, b^\circ$ ) $\theta^\circ$	ds=45' ( $\ell^\circ, b^\circ$ ) $\theta^\circ$
$l = [20, 240]$	(253.0,20.0) 29.4	(258.9,19.7) 28.6	(265.1,22.6) 25.4	(267.4,22.8) 25.4
	(266.5,28.3) 19.8	(268.8,28.8) 19.5	(274.5,30.0) 19.8	(274.6,30.7) 19.1
	(271.9,33.7) 15.5	(273.9,34.9) 15.1	(283.6,35.1) 19.4	(284.5,36.0) 19.2
$l = [60, 240]$	-	(259.3,25.4) 22.8	(266.5,28.5) 19.6	(269.2,28.4) 20.0
	-	(265.6,37.9) 10.2	(271.3,38.9) 10.5	(271.1,39.2) 10.2
	-	(272.4,45.1) 6.5	(284.1,44.9) 14.1	(285.9,45.4) 15.2
$l = [100, 240]$	-	(264.6,40.2) 7.8	(269.3,42.6) 6.5	(270.9,42.9) 7.0
	-	(266.2,52.6) 4.8	(273.7,53.8) 8.4	(274.7,52.5) 8.2
	-	(279.4,54.6) 11.6	(288.4,54.1) 16.4	(289.4,54.1) 17.0

Table 2: The dipole direction of LV maps obtained in the current study using  $P$ -masks, but utilizing various filtered  $E$ -maps and disc radii. Their amplitudes are listed in Table [1]. The three sub-rows in each horizontal block correspond to using the masks `mask074`, `mask080` and `mask085` respectively.  $(\ell, b)$  (in degrees) correspond to the dipole directions in galactic coordinates, and  $\theta = \text{acos}(\hat{d}_{LV} \cdot \hat{d}_{CMB})$ , where  $\hat{d}_{LV}$  is the dipole direction of a local variance map and  $\hat{d}_{CMB}$  is the CMB kinetic dipole direction.  $\theta$  denotes an LV dipole axis's proximity to the CMB kinetic dipole. The angles are given in degrees ( $^\circ$ ).

shown in *top panel* of Fig. [4]. They broadly point towards the CMB kinetic dipole. The dipole directions inferred from data when using galactic mask with larger sky fraction are aligned more closely towards CMB dipole. This suggests that the normalized LV maps' dipole axes are sensitive to the available sky fraction in the mask used, and consequently to the residual contamination. still present in the CMB  $E$ -map. Various LV maps' dipole directions ( $\hat{d}_{LV}$ ) are listed in *top* block of Table [2] along with the axes proximity to the CMB kinetic dipole ( $\hat{d}_{CMB} = (\ell^\circ, b^\circ) = (264^\circ, 48^\circ)$  [38]) direction measured as  $\theta = \text{acos}(\hat{d}_{LV} \cdot \hat{d}_{CMB})$ .

Now we check whether there is any significant power in modes other than dipole in the local variance maps. This would inform us whether the anomalous power asymmetry we found is only dipolar in nature or other modes are also contributing to the observed power asymmetry. We find that there is significant power only in the dipole component of the local variance maps from polarization data. As an example, in Fig. [5], we show the angular power spectrum plot of local variance map derived using the range  $l = [20, 240]$  from data, and estimated using disc radius of 60' (arcmin) and the galactic mask `mask074`. We applied the first order  $f_{sky}$  correction to estimate the angular power spectrum,  $C_L$ , where  $L$  is the multipole index of LV maps.

Thus we find a signal of anomalous dipole power asymmetry in CMB  $E$ -mode polarization maps from PLANCK full mission data on large angular scales, broadly pointing in the CMB kinetic dipole direction. The dipole axis inferred is however found to be sensitive to the galactic mask, used to estimate the LV maps from the current release of polarization data.

## 4.2 Scale dependence of amplitude of dipolar power asymmetry

In this section we probe the dipole power asymmetry signal at small angular scales. This will allow us to evaluate any scale dependence in the amplitude of the dipole modulation signal we are studying in CMB  $E$ -mode polarization maps. Given the limited number of circular disc radii we could use with the current data, we exclude the large angular scales in progression to study any such scale dependence with local variance maps.

To this end, we use two filtered CMB  $E$ -mode maps containing small angular scales ie., comprising the multipoles  $l = [60, 240]$  and  $l = [100, 240]$ . A high and low pass filters defined in Eq. [10] and [11] are applied over a width of 20 multipoles at both ends of the multipole ranges mentioned for the two filtered maps. Since these maps contain smaller angular scales, we use

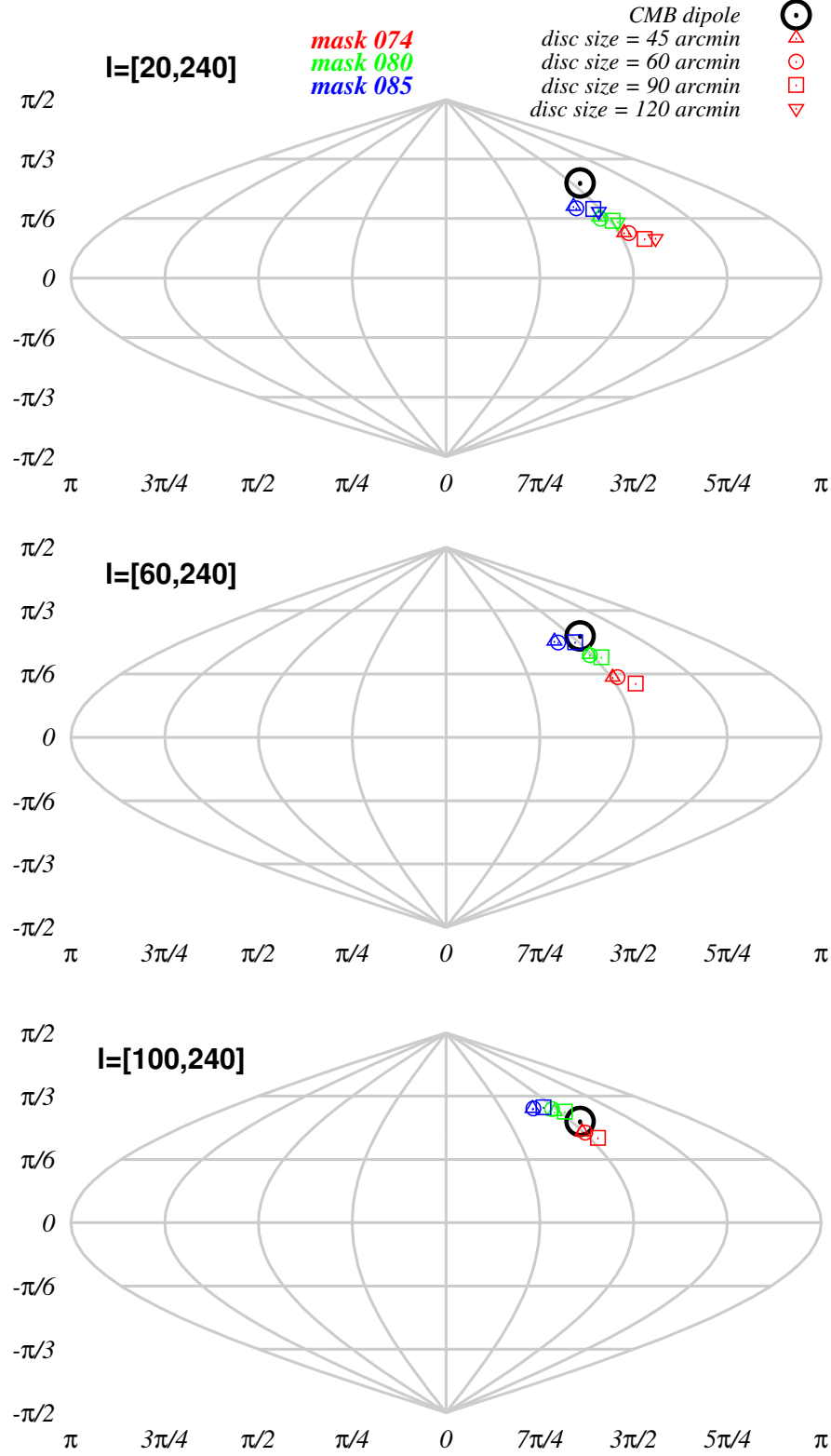


Figure 4: Dipole directions inferred from normalized local variance maps of  $E$ -mode CMB map from PLANCK full mission observations, specifically obtained using the **Commander** component separation algorithm, are shown here in galactic co-ordinates. *Top*, *Middle* and *Bottom* panels correspond to direction of dipoles as recovered from three different filtered  $E$ -maps (ie., studying different angular scales) as indicated. The *red*, *green*, and *blue* points in each panel denotes the dipole direction from LV maps as estimated using different masks with different sky fractions. The coloured *up triangle*, *circle*, *square* and *inverted triangle* point types correspond to the four chosen circular disc radii, 45', 60', 90' and 120' (arcmin), for computing local variances.

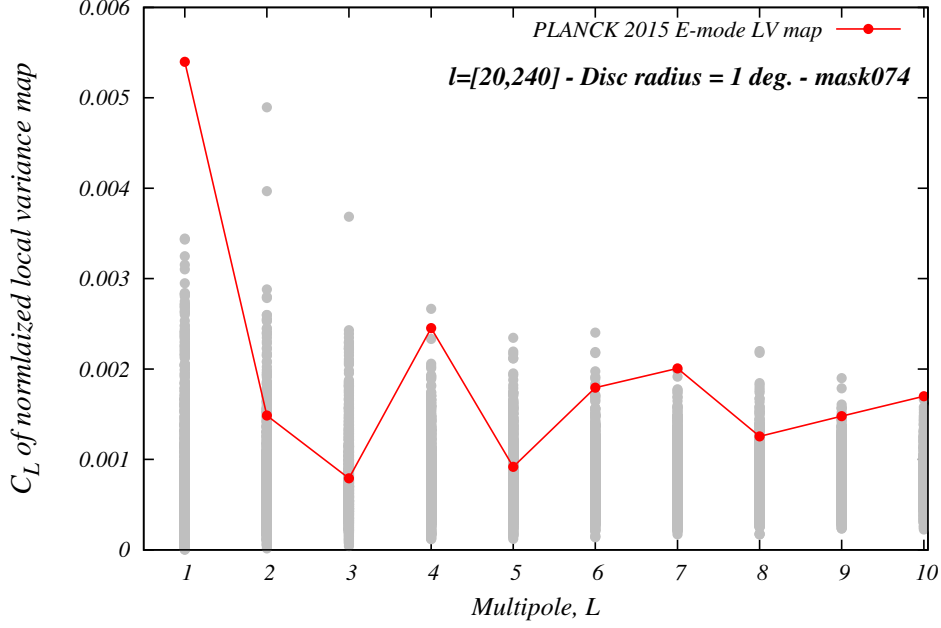


Figure 5: Angular power spectrum of local variance map obtained using  $E$ -mode CMB map from PLANCK’s **Commander** 2015 CMB estimate, comprising the multipole  $l = [20, 240]$ . Specifically a circular disc of  $60'$  (arcmin) radius and **mask074** were used. We see a significant power in only the  $L = 1$  mode. This example plot illustrates that the power asymmetry signal seen in polarization data is entirely dipolar in nature. The grey dots against each multipole,  $L$ , denote simulation estimates, and the red line with red point type denotes angular power spectrum of LV map from data as indicated.

only three circular discs of radii  $90'$ ,  $60'$  and  $45'$  (arcmin) to get LV maps. The three  $P$ -masks shown in Fig. [2] are used as in the previous section. We again demand availability of at least 90% of pixels in the effective circular discs, defined as union of the galactic masks and the full circular discs defined locally on **HEALPix**  $N_{\text{side}} = 64$  grid to map local variances.

The amplitude of dipole of normalized local variances maps from the two filtered CMB  $E$ -mode maps are shown in Fig. [6]. The plots in left-hand column of the figure corresponds to using the filtered map containing  $l = [60, 240]$ , and the right-hand column corresponds to those comprising  $l = [100, 240]$ . Each plot has again three histograms in *red*, *green* and *blue* corresponding to use of **mask074**, **mask080** and **mask085** galactic masks. The data values are denoted by triangle point types in each plot. The three rows in Fig. [6] correspond to results obtained using the three disc radii  $90'$ ,  $60'$  and  $45'$  (arcmin).

One can see that, the amplitude of dipole in LV maps is anomalous only when obtained from the range  $l = [60, 240]$ . The dipole amplitudes in the LV maps from the filtered  $E$ -map containing  $l = [100, 240]$  modes are consistent with amplitude excursions expected in isotropic maps. The dipole power asymmetry amplitudes and their  $p$ -values corresponding to the two filtered maps are listed in the *second* and *third* block of Table [1]. The corresponding dipole directions are shown in the *middle* and *bottom* panel of Fig. [4]. These dipole directions are still broadly pointing towards CMB Doppler boost direction, nearly independent of the choice of disc radius and galactic mask used. But the orientation of the dipole axes move towards higher latitudes around the kinetic dipole axis by excluding low multipoles. The dipole directions corresponding to LV maps from these two filtered CMB  $E$ -mode maps are listed in the *second* and *third* block of Table [2], along with their angular separation from the CMB kinetic dipole direction.

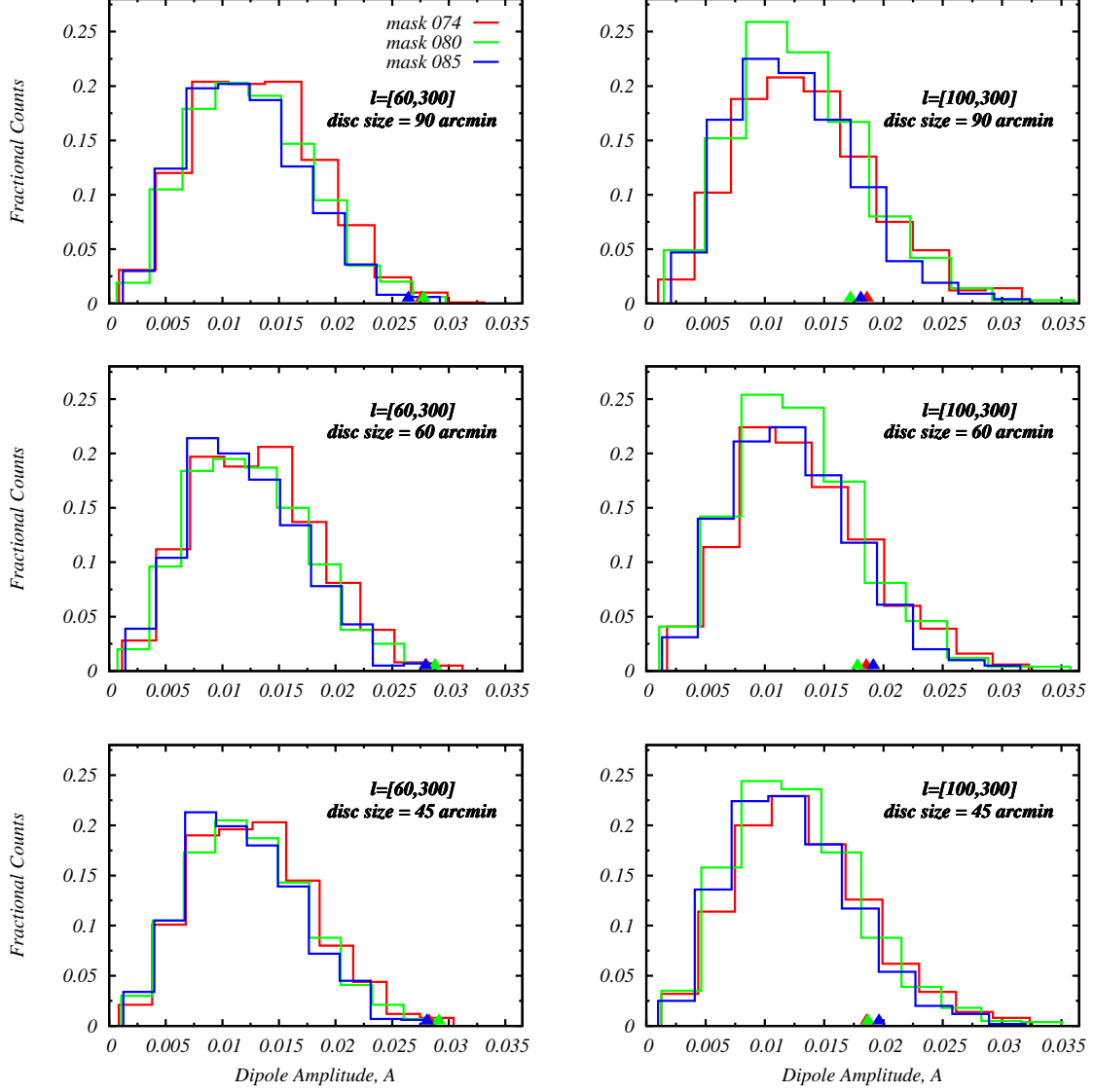


Figure 6: Same as Fig. [3], but for normalized local variance maps obtained using the mutlipole range  $l = [60, 240]$  and  $l = [100, 240]$  (the two columns), and local circular disc radii of radii 90', 60' and 45' (arcmin) (the three rows). Each plot has three histograms that correspond to estimating the dipole amplitudes with three different  $P$ -masks as labelled.



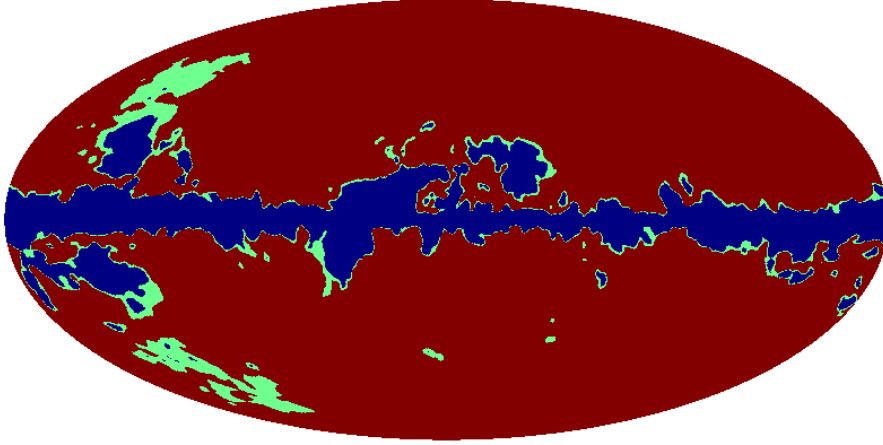


Figure 7: The two  $E$ -mode masks viz., `mask080E` (red only) and `mask085E` (light green+red) are shown here. The blue region is commonly excluded by both masks.

### 4.3 LV analysis using $E$ -mode mask

Here we redo the exercise of local variance analysis described in the preceding sections, using  $E$ -mode masks. So far we used masks derived in  $Q/U$  basis ie.  $P$ -masks, where  $P^2 = Q^2 + U^2$ . Now we repeat the LV analysis using  $E$ -mode foreground masks created as described below, as a test of consistency of our results obtained using  $P$ -maps.

Once we obtain the difference maps 030-070 and 353-070 from raw PLANCK stokes  $Q/U$  satellite maps, as described in Sec [3.2.2], we convert these difference maps into  $E$ -mode maps which contain only foregrounds. The two  $E$ -mode difference maps are combined to form a *junk map*, where we retain only the largest absolute pixel-value, among the two, in the output *junk map*, following the procedure of Tegmark et al. (2003) [37]. This map is then thresholded such that the resultant masks contains  $f_{sky} \approx 80\%$  and  $85\%$  ie., unmasked sky fractions. The masks thus obtained, denoted here after as `mask080E` and `mask085E`, are shown in Fig. [7].

We now go on to estimate the local variance maps using these  $E$ -mode masks. The analysis procedure is same as described in Sec. [4.1], except for using the newly derived  $E$ -masks. Here we only analyze the filtered  $E$ -mode CMB map that includes the large angular scales ie., the data  $E$ -maps containing the full range  $l = [20, 240]$ , and also use a single disc radius of  $120'$  (arcmin) to compute local variances.

The dipole amplitudes derived by fitting a dipole to normalized local variance maps in this case are shown in *left-hand* panel of Fig. [8] in comparison to simulations. The two histograms in that panel correspond to the two  $E$ -masks used, and the data points are denoted by triangle point types. The direction of the dipole as inferred from these normalized data LVE maps are shown in the same figure in the *right-hand* panel. The observed dipole amplitudes and their significances using `mask080E` and `mask085E` are tabulated in Table 3.

The dipole amplitudes now obtained using  $E$ -space masks are found to be lower in amplitude than those obtained when using  $P$ -masks in Sec. [4.1]. Their significances have become  $0.3\%$  and  $0.1\%$ , respectively, when `mask080E` and `mask085E` are used. The dipole directions now seem to be more closely aligned with the CMB kinetic dipole direction. For reference, the dipole directions from using the  $P$ -masks viz., `mask080` and `mask085` with the same circular radius of  $120'$  (arcmin) to obtain LV maps are also indicated in the right panel of Fig. [8].

## 5 Conclusions

In this paper, we tried to probe the presence of hemispherical power asymmetry in CMB  $E$ -mode polarization data, that was so far studied in CMB temperature data. To this end

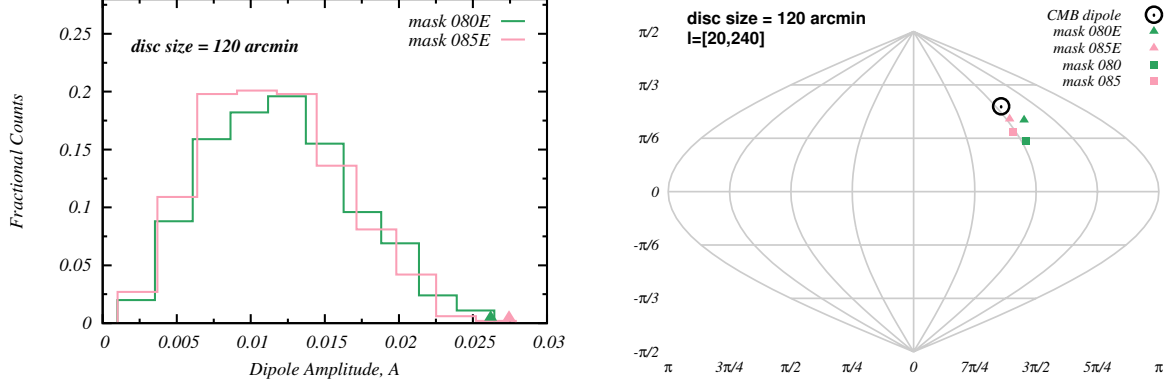


Figure 8: *Left* : Histograms of dipole amplitudes obtained from simulations in comparison to data derived values, when using `mask080E` and `mask085E` are shown here. *Right* : Dipole directions inferred from normalised LVE maps obtained using the two  $E$ -space masks and the filtered  $E$ -mode data CMB map containing the large angular scales ( $l = [20, 240]$ ) are shown here. These LV maps are estimated using  $120'$  (arcmin) radius circular discs, to compute local variances. For comparison, the dipole directions shown in the top panel of Fig. [4] corresponding to LVE maps obtained using CMB  $E$ -map with  $l = [20, 240]$ , and employing the  $P$ -masks viz., `mask080` and `mask085` and circular radius of  $120'$  (arcmin) are also plotted.

mask	$A$	$p$ -value	$\hat{d}_{LV} = (\ell^\circ, b^\circ)$	$\theta^\circ = \arccos(\hat{d}_{LV} \cdot \hat{d}_{CMB})$
<code>mask080E</code>	0.026(10)	0.003	(253.7, 40.2)	10.7
<code>mask085E</code>	0.027(9)	0.001	(266.8, 40.8)	7.5

Table 3: Dipole amplitude ( $A$ ) and significances ( $p$ ) derived from LVE maps obtained using PLANCK Commander  $E$ -mode CMB map, and the `mask080E` and `mask085E` confidence masks, are tabulated here. The CMB  $E$ -map contains the multipoles  $l = [20, 240]$  and a local circular discs of radius  $120'$  (arcmin) were used to compute variances. Also given are the direction of LV dipoles ( $\hat{d}_{LV}$ ) and their angular distance from CMB Doppler direction, both in degrees.

we used Stokes  $Q/U$  CMB maps from PLANCK full mission data estimated using **Commander** component separation procedure. From these full-sky Stokes  $Q/U$  maps available at **HEALPix**  $N_{side} = 1024$  and having a Gaussian beam smoothing of  $FWHM = 10'$  (arcmin), we derived  $E$ -mode polarization map of CMB. This  $E$ -mode map is obtained at a low resolution of  $N_{side} = 256$  and with a smoothing given by a Gaussian beam of  $FWHM = 40'$  (arcmin). The low resolution  $E$ -mode map is further low-pass and high-pass filtered to get three maps comprising different ranges of multipoles viz.,  $l = [20, 240]$ ,  $[60, 240]$  and  $[100, 240]$  to test for any scale dependence of the amplitude of hemispherical power asymmetry modelled as dipole modulation.

We find a tentative evidence for the presence of dipole modulation in polarization data as well, with an amplitude of  $\sim 2.6\% - 3.9\%$  depending on the mask, and disc radius used on large angular scales (ie., using the multipole range  $l = [20, 240]$ ). The lower values are found when  $E$ -space masks are used for computing local variance maps, instead of  $P$ -masks where  $P^2 = Q^2 + U^2$ . This sheds light on some important analysis aspect that the mask used for analyzing CMB  $E$ -mode maps have to be constructed carefully, and the  $P$ -masks that are provided with second PLANCK data release may not be readily applicable in  $E$ -space. LV maps from intermediate and small angular scales of the CMB  $E$  polarization map considered in the present work are found to have lower dipole amplitude. The amplitude of the dipoles on large angular scales were found to be very significant with a probability of  $p < 1/1000$ , which goes down to  $p \sim 0.2$  on small angular scales. The direction of the dipoles inferred from fitting a dipole to the local variance maps are found to be roughly pointing towards the CMB kinetic dipole direction, and broadly independent of the angular scales involved, and masks and circular disc radii used to obtain LV maps. The dipole axis inferred when using  $E$ -space masks are found to be more closely aligned with the CMB dipole direction.

However, with the know issue of systematic artefacts on large angular scales of PLANCK polarization data, only precise future measurements of polarization or a future PLANCK polarization data release with carefully processed large angular scales will validate these findings, beyond any systematics still present in the multipole range studied here.

## Acknowledgements

We are very thankful to Anthony Banday for a careful reading of our draft and giving his valuable comments. We also thank Changbom Park for helpful discussions. P.K.A. and A.S. would like to acknowledge the support of the National Research Foundation of Korea (NRF-2016R1C1B2016478). The present work has extensively made use of the publicly available **HEALPix**<sup>6</sup> [39] package, a frame work for representing data on a sphere and to perform additional manipulations thereof. Part of the results presented here are based on observations obtained with PLANCK<sup>7</sup>, an ESA science mission with instruments and contributions directly funded by ESA Member States, NASA, and Canada.

## References

- [1] Eriksen H. K., Hansen F. K., Banday A. J., Gorski K. M., & Lilje P. B., 2004, ApJ, 605, 14
- [2] Bennett C. L. et al., 2011, ApJS, 192, 17
- [3] Planck Collaboration : Ade P. A. R. et al., 2014, A & A, 571, A23
- [4] Planck Collaboration : Ade P. A. R. et al., 2016, A & A, 594, A16

---

<sup>6</sup><https://healpix.jpl.nasa.gov/>

<sup>7</sup><http://www.esa.int/Planck>

- [5] Hansen F. K., Banday A. J., & Gorski K. M., 2004, MNRAS, 354, 641
- [6] Hajian A., Souradeep T., & Cornish N., 2005, ApJL, 618, L63
- [7] Prunet S., Uzan J. P., Bernardeau F., & Brunier T., 2005, Phys. Rev. D, 71, 083508
- [8] Armendariz-Picon C., 2006, JCAP, 03, 002
- [9] Eriksen H. K., Banday A. J., Gorski K. M., Hansen F. K., & Lilje P. B., 2007, ApJL, 660, L81
- [10] Bernui A., Mota B., Reboucas M. J., & Tavakol R., 2007, IJMPD, 16, 411
- [11] Lew B., 2008, JCAP, 09, 023
- [12] Bernui A., 2008, Phys. Rev. D, 78, 063531
- [13] Hansen F. K., Banday A. J., Gorski K. M., Eriksen H. K., & Lilje P. B., 2009, ApJ, 704, 1448
- [14] Hanson D., & Lewis A., 2009, Phys. Rev. D, 80, 063004
- [15] Paci F. et al., 2010, MNRAS, 407, 399
- [16] Paci F. et al., 2013, MNRAS, 434, 3071
- [17] Flender S., & Hotchkiss S., 2013, JCAP, 09 033
- [18] Rath P. K., & Jain P., 2013, JCAP, 12, 014
- [19] Santos L. et al., 2014, A & A, 569, A75
- [20] Akrami Y. et al., 2014, ApJL, 784 L42
- [21] Bernui A., Oliveira A. F., & Pereira T. S., 2014, JCAP, 10, 041
- [22] Adhikari S., 2015, MNRAS, 446, 4232
- [23] Quartin M., & Notari A., 2015, JCAP, 01, 008
- [24] Aiola S., Wang B., Kosowsky A., Kahniashvili T., & Firouzjahi H., 2015, Phys. Rev. D, 92, 063008
- [25] Ghosh S., Kothari R., Jain P., & Rath P. K., 2016, JCAP, 01, 046
- [26] Gordon C., Hu W., Huterer D., & Crawford T., 2005, Phys. Rev. D, 72, 103002
- [27] Gordon C., 2007, ApJ, 656, 636
- [28] Planck Collaboration: Adam R. et al., 2016, A & A, 594, A9
- [29] Goldberg J. N., et al., 1967, Jou. Math. Phys., 8, 2155
- [30] Zaldarriaga M., Seljak U., 1997, Phys.Rev. D, 55, 1830
- [31] Kamionkowski M., Kosowsky A., Stebbins A., 1997, Phys.Rev. D, 55, 7368
- [32] Zaldarriaga M., 1998, ApJ, 503, 1
- [33] Shafieloo, A., Clifton, T. & Ferreira, P. 2011, JCAP, 9, 017
- [34] Colin, J., Mohayaee, R., Sarkar, S., & Shafieloo, A. 2011, MNRAS, 414, 264

- [35] Shafieloo, A. 2012, JCAP, 5, 024
- [36] Shafieloo, A. 2012, JCAP, 8, 002
- [37] Tegmark M., de Oliveira-Costa A., Hamilton A. J., 2003, Phys. Rev. D, 68, 123523
- [38] Kogut A. et al., 1993, ApJ, 419, 1
- [39] Gorski K. M. et al., 2005, ApJ, 622, 759
- [40] Hivon E. et al., 2002, ApJ, 567, 2

## Appendix

### A Treatment of noise simulations

As described in Sec. [3.2.3], effective noise realizations were obtained using co-addition of smoothed, downgraded frequency specific FFP8 noise maps. However the noise levels in polarized FFP realizations were under estimated compared to data. One can use the half-mission half-difference (HMHD) map from the two **Commander** polarized CMB maps derived using half mission data as proxy to the true noise level in PLANCK **Commnader**  $E$ -mode CMB map. These half-mission maps are also provided through PLANCK second public release<sup>8</sup>. This HMDH map is processed in the same way as the data CMB  $E$ -mode polarization map, to get a low resolution version.

Here we compare the noise levels in simulations and data, in an attempt to be able to use the FFP polarization noise simulations with reasonable modifications. To reliably derive the noise angular power spectrum from **Commnader** polarized HMHD maps, and from the FFP8 polarized noise simulations, we have to first modify the masks shown in Fig. [2]. The half-mission (HM) data itself comes with additional mask owing to missing pixels in respective data sets, that is further processed and downgraded to  $N_{side} = 256$ . The original half-mission mask is made available at  $N_{side} = 1024$ . To this we also add the missing pixels mask from single year maps to make it more conservative. This combined mask is downgraded to  $N_{side} = 256$  and smoothed with a Gaussian beam of  $FWHM = 40'$  (arcmin). Then a pixel cut-off of 0.95 is imposed whereby pixels with pixel-value greater than this are set to '1' and rest to '0'. The mask thus obtained is shown in Fig. [9].

The three  $P$ -masks shown in Fig. [2] are then taken in *union* with the suitably extended, downgraded half-mission mask of Fig. [9]. However in order to compute the noise power spectrum from partial sky, it would be useful to apodize the masks to avoid ringing in the recovered noise power spectra due to sharp mask boundaries (the so-called Gibbs phenomenon). So we use a *cosine* profile to apodize the three *union* (galactic+HM) masks over a width of  $200'$  (arcmin) at the mask boundaries. Recall that these masks are at  $N_{side} = 256$ , which have pixels of side  $\sqrt{4\pi/(12 \times 256^2)} \approx 13.74'$  (arcmin), assuming them to be square shaped. So, choosing to apodize over a width of 10 pixels strips along the mask boundary equals an apodization width of  $\sqrt{2} \times 13.74' \times 10 \approx 194.3'$ .

These apodized union masks are used to mask the **Commander** HMHD  $E$ -mode map. Then the pseudo full-sky noise power spectra were obtained following the MASTER algorithm [40]. We repeat the same exercise on 1000 FFP8 co-added noise polarization maps by applying the union masks with differing sky fractions. A comparison of respective power spectra is shown in *top panel* of Fig. [10]. For brevity only the pseudo full-sky noise power spectrum from using the union mask **mask074+HM** on data and simulations is shown in that panel.

<sup>8</sup>[http://irsa.ipac.caltech.edu/data/Planck/release\\_2/all-sky-maps/matrix\\_cmb.html](http://irsa.ipac.caltech.edu/data/Planck/release_2/all-sky-maps/matrix_cmb.html)

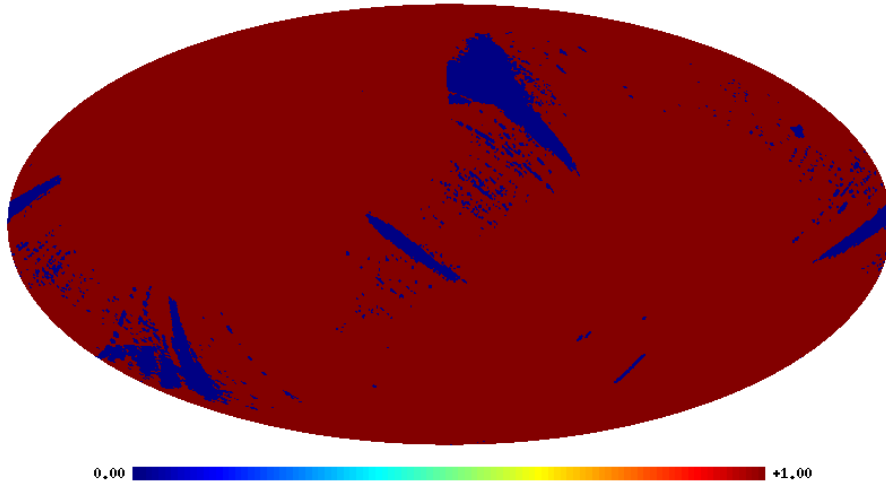


Figure 9: Half-mission mask that is suitably extended to  $N_{side} = 256$  is shown here. The original mask is provided at HEALPix  $N_{side} = 1024$ . See text for details.

In the *bottom panel* of Fig. [10], we show the ratio of pseudo full-sky noise power spectrum from **Commander** HMHD  $E$ -mode map ( $N_l^{HMHD}$ ) to the corresponding mean pseudo full-sky noise spectrum from 1000 effective FFP noise maps ( $\langle N_l^{FFP8} \rangle$ ), obtained using the three union masks. Also shown is the mean of the three noise power spectra ratios (as dark green solid line), smoothed using a running window of  $\Delta l = 21$  (ie., average over  $l \pm 10$  at each multipole,  $l$ ). We find that this mean of the ratio of noise power spectra is approximately constant upto  $l = 240$ . By taking the average of all three noise power spectra ratios in the range  $l = [41, 240]$  we get a factor  $\approx 1.74$ , that is plotted as a black dashed curve in the same figure (bottom panel). Thus we scale the effective noise maps by a factor of  $\sqrt{1.74} \approx 1.32$  to alleviate their noise levels in comparison to true noise in data maps.

As explained in Sec. 4.3, we devised additional masks directly in  $E$ -space. Since the  $P$ -masks we used have varying mask fractions, we expect the scaling factor found with them to still hold when estimated using  $E$ -masks. Nevertheless, we analyzed the HMHD noise proxy using **mask085E** (see Fig. [7]) following the same procedure as with  $P$ -masks. We find the ratio of the **Commander** HMHD to mean simulation noise power spectra obtained by employing **mask085E** to have a similar level of mismatch, and also result in approximately same factor of 1.32 for scaling the simulations.



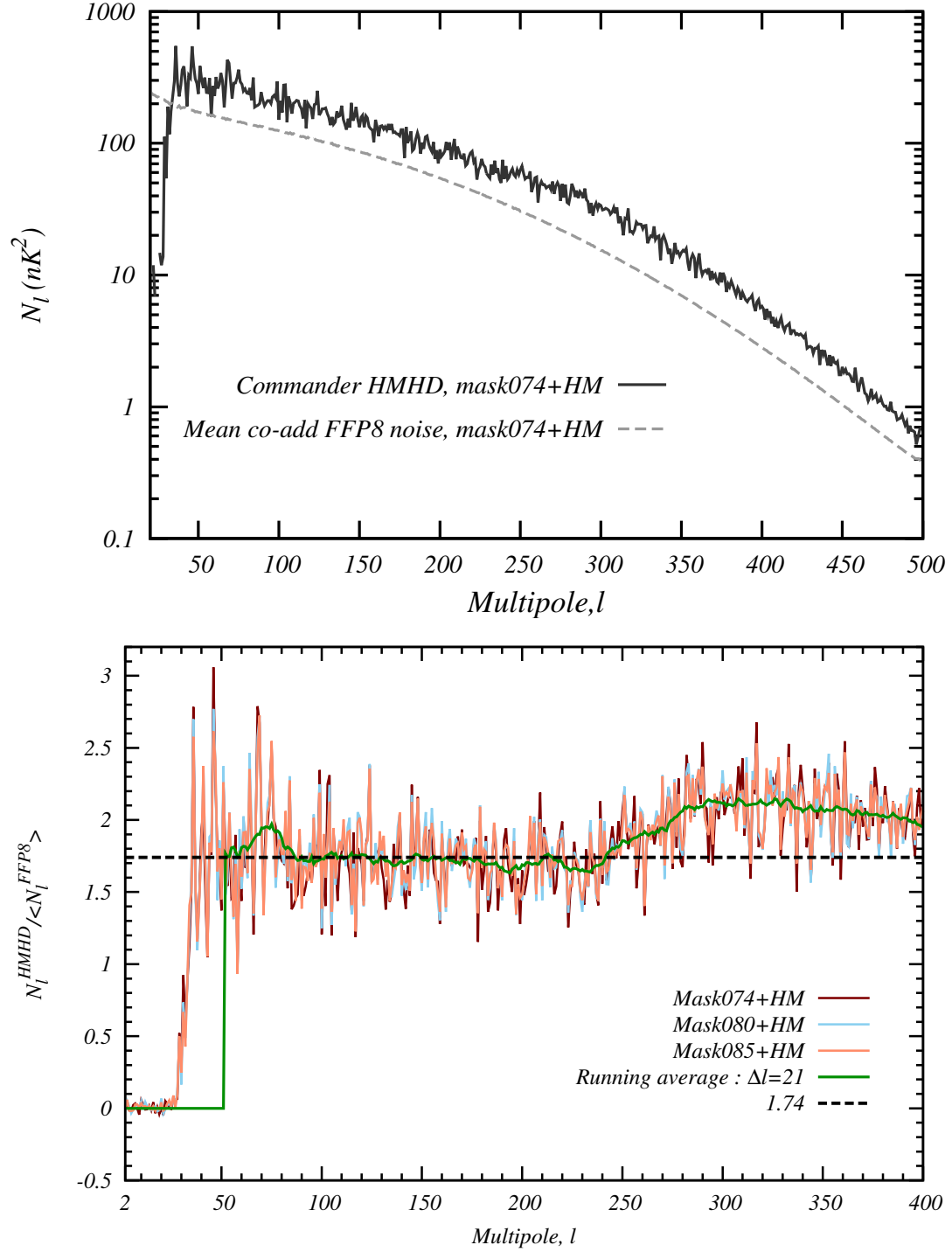


Figure 10: Comparison of noise levels in polarization data and FFP8 simulations are shown here, obtained using the three galactic masks shown in Fig. [2], taken in union with the half-mission mask of Fig. [9]. In practice, apodized versions of the said masks were used to compute the noise power spectra.